Supporting Information for "Ice shelf basal melt rates in the Amundsen Sea at the end of the 21st century"

Nicolas C. Jourdain[1], Pierre Mathiot[1], Clara Burgard [1], Justine Caillet[1],

Christoph Kittel[1]

[1]Univ. Grenoble Alpes/CNRS/IRD/G-INP, Institut des Géosciences et de l'Environnement, Grenoble, France

Contents of this file

1. Supplementary sections S1 to S4.
2. Figures S1 to S6.
3. Table S1.

Corresponding author: N. C. Jourdain, Institut des Géosciences de l'Environnement, University Grenoble Alpes, CS 40700, 38 058 Grenoble Cedex 9, France. (nicolas.jourdain@univ-grenoble-alpes.fr)

Introduction

Here we present additional diagnostics that help support the main manuscript. They include comparison of our simulations to observational estimates (section S1), a description of future changes regarding sea ice, Ekman pumping and the surface buoyancy fluxes (section S2), a description of the future anomalies applied at the model lateral boundaries (section S3), and a description of the heat and salt budgets northward of the Amundsen continental shelf (section S4).

S1. Evaluation of the present day simulations

We first evaluate the vertical temperature and salinity profiles in front of the most important ice shelf cavities (Fig. S1). The observations come from in-situ Condictivity-Temperature-Depth (CTD) measurements over 1994-2018 (Dutrieux et al., 2014; Jenkins et al., 2018). The three model ensemble members (A, B, C) have slightly different properties (e.g., C is less stratified), but their biases with respect to observations are very similar. NEMO generally has a warm bias below the thermocline, of approximately 0.5°C for Pine Island, Thwaites and Getz, and up to 1°C for Dotson. The model thermocline tends to be too shallow, and the bias is particularly strong for Getz where the model thermocline is ∼200 m above the observed one.

We then evaluate the simulated cavity melt rates in comparison to oceanographic and remote-sensing observational estimates (Fig. S2). The simulated melt rate at Pine Island is in good agreement with observational estimates. Thwaites melt rates appear strongly under-estimated, but its recent geometry is used in our simulations while observational estimates were done before its partial collapse. For the other ice shelves, simulated melt

rates are overestimated, consistently with the aforementioned warm bias at depth. The melt bias is particularly important for Getz because the overly shallow thermocline at its front exposes large areas of ice to modified circumpolar deep water instead of surface water.

S2. Future changes in sea ice cover, Ekman pumping and buoyancy fluxes

Here we describe the changes at the ocean surface, first in terms of sea ice concentration and thickness, then in terms of Ekman pumping and surface buoyancy fluxes which are the main external drivers of changes in the ocean circulation.

Nearly 90% of the present-day austral summer (January to March) sea ice concentration over the Amundsen Sea continental shelf disappears in the future (Fig. S3a,b). There is a strong retreat of the main sea ice front in austral winter, but the sea ice concentration remains mostly unchanged between the present and the future over the Amundsen continental shelf (Fig. S3c,d). The winter sea ice thickness is nonetheless reduced, from 1.28 m on average for present day to 0.85 m in the future over the continental shelf (Fig. S3e,f). The annual net sea ice production over the continental shelf (which matters for ocean convection) decreases from 231 $\mathrm{Gt\,yr^{-1}}$ presently to 194 $\mathrm{Gt\,yr^{-1}}$ in the future (not shown).

The Ekman vertical velocity (w_E) is calculated as:

$$w_E = -\frac{1}{\rho_w} \nabla \times \left(\frac{\vec{\tau}}{f} \right) \tag{1}$$

where ρ_w is the seawater density (1028 $\mathrm{kg.m^{-3}}$), τ the ocean surface friction (exerted by wind and sea ice), and f the Coriolis parameter. The multiple dipole-like structures in the Ekman velocity (Fig. S4a) correspond to relatively intense surface currents that feel

the sea ice drag, with opposite friction curl on either side of the currents. These dipoles tend to be weakened in the future (Fig. S4b), possibly because of the reduced sea ice cover and thickness. On average, the Amundsen continental shelf experiences an Ekman downwelling (see number in Fig. S4a) that is reduced by half in the future simulations (see number in Fig. S4b).

The surface buoyancy flux is calculated as:

$$B = \frac{g}{c_{pw}} \alpha_{T,S} Q + g S \beta_{T,S} F \tag{2}$$

where g is the gravity acceleration (9.81 $\mathrm{m\,s^{-2}}$), c_{pw} the seawater specific heat capacity (3992 $\mathrm{J\,K^{-1}\,kg^{-1}}$), T and S the conservative temperature and absolute salinity at the ocean surface, $\alpha_{T,S}$ the thermal expansion coefficient at constant salinity, $\beta_{T,S}$ the saline contraction coefficient at constant temperature, Q the net heat flux received by the ocean surface (from the atmosphere and sea ice), and F the net freshwater flux at the ocean surface, positively influenced by precipitation, iceberg melt, sea ice melt and runoff (neglected in our study), and negatively influenced by evaporation and sea ice formation. On average, for present day, the Amundsen Sea is loosing surface buoyancy (Fig. S4c), which is due to sea ice production, particularly in coastal polynyas, which is not fully compensated by sea ice melt as the later occurs further offshore due to sea ice drift. In the future, less sea ice is produced and there is more precipitation, which weakens the annual buoyancy loss by 75% on average for the Amundsen Sea (Fig. S4d).

S3. Future ocean changes at the lateral boundaries

Here we describe the ocean perturbation applied at the lateral boundaries of our ocean model configuration as it significantly impacts future ice shelf melt rates.

The ocean warming imposed at the lateral boundaries generally exceeds 0.25°C in the first 1000 m and 0.5°C in the first 500 m (Fig. S5a). This is approximately in agreement with the 0.4°C warming of Circumpolar Deep Water (CDW) in the CMIP5 multi-model mean under RCP8.5 (Sallée et al., 2013). As argued by Sallée et al. (2013), vertical mixing is likely responsible for such warming because advection from the CDW formation regions is expected to take several centuries. The imposed warming is also slightly stronger throughout the water column on the continental shelf on both sides of the lateral boundaries, with warming amplitude consistent with the +0.66°C reported by Little and Urban (2016) for the Amundsen Sea under RCP85. This may indicate some additional Ekman dynamics (reduced downwelling) related to poleward shifted westerlies in the future (Spence et al., 2014).

A slight freshening of the first 100 m is also imposed along most of the lateral boundaries (Fig. S5b), with a weak signal also reported by Sallée et al. (2013). The anomaly is much stronger and deeper on the continental shelf on both sides of the lateral boundaries, exceeding -0.3 and -0.6 $g.kg^{-1}$ at the western and eastern boundaries, respectively. The deep vertical structure is again consistent with reduced downwelling in response to poleward shifted winds (Spence et al., 2014). This freshening signal near Antarctica is also likely related to the increased glacial freshwater flux from the Antarctic ice sheet (the later was crudely represented in CMIP5; for example, some modelling centers increased the glacial freshwater fluxes into the Southern Ocean to instantaneously compensate for greater snow accumulation over the ice sheet in a warmer climate).

In terms of perturbed ocean velocities, we find a westward anomaly near the continental shelf, as previously reported by Wang (2013). The anomaly structure is similar to the typical Antarctic Slope Current. The relatively weak anomalies probably result from the large spread of dynamical responses across the CMIP5 models (Wang, 2013; Meijers et al., 2012).

S4. Estimation of future iceberg melt rates

The ISMIP6 results indicate that for each 1 Gt of additional melt beneath the East-Amundsen ice shelves (Cosgrove, Pine Island, Thwaites, Crosson and Dotson) there will be 0.72 Gt of additional calving from these ice shelves (Seroussi et al., 2020, , their Fig. 15). For Getz ice shelf, each 1 Gt of additional melt induces 0.18 Gt of additional calving. We apply these sensitivities to the increased ice-shelf basal melt rates in our simulations and deduce an increase in calving rates (2nd part of Tab. S1). With respect to the present-day values of Depoorter et al. (2013), this corresponds to 67 to 103% of additional calving in the Crosson-Dotson sector, and to 39 to 64% of additional ice calved by Getz (3rd part of Tab. S1).

Analysing the tracks of Lagrangian icebergs in the global 0.25° simulation used as lateral boundary conditions of our regional simulations, we find that only 14% of the iceberg mass calved in the Amundsen Sea does melt in the Amundsen Sea. Most of them actually melt farther away, in the Antarctic Circumpolar Current. It means that the total iceberg melt flux in the Amundsen Sea is not only controlled by the calving rate, but also by the melt intensity when icebergs travel across the Amundsen Sea. To estimate the effect of more intense melting, we use the iceberg model equations (Martin & Adcroft, 2010)

and consider that surface water temperatures increase from -1.5°C to -1.0°C (based on our NEMO simulations). The response is dominated by increased wave erosion (+100%), while increased melting at the iceberg base (+20%) is nearly compensated by decreased convection along the iceberg side walls (-26%). We note that the equation provided by Martin and Adcroft (2010) for melt induced by convection along the iceberg side walls may not be realistic for negative ocean temperatures and should probably be based on the ocean salinity, but this term does not have an important impact on our overall estimate.

Therefore, we estimate that the relative increase in iceberg melt rate compared to present-day (4th part of Tab. S1) is the sum of the relative increase in calving and of the relative increase in wave erosion. The maximum response across the 3 ensemble members is an additional 203% melting for icebergs coming from the Cosgrove-Dotson sector and an additional 164% for icebergs coming from Getz.

As we saved the original iceberg melt flux per sector of origin, we are able to multiply by 3.03 the pattern of iceberg melt coming from the Eastern Amundsen Sea and by 2.64 the pattern of iceberg melt coming from the Western Amundsen Sea. This affects only 44% of the present-day iceberg melt flux in the Amundsen Sea as 41% comes from icebergs calved in the Bellingshausen Sea, 12% come from the Ross Sea, and 3% from the Adélie Land (estimates for the Amundsen continental shelf between 135°W and 100°W). We assume that these other sectors do not change in the future because there is a weaker calving to basal melt relationship compared to Amundsen sector (Seroussi et al., 2020), and because increased iceberg erosion by the ocean may decrease their ability to be transported far away. The resulting total iceberg melt flux over the Amundsen continental shelf increases

from 63 Gt yr−1 at present-day to 136 Gt.yr^{-1} at the end of the 21st century under RCP85.

S5. Description of the offshore projected changes

Here we analyse the offshore properties and the terms of the exact heat and salt budget (saved online and calculated as in Jourdain et al., 2017) to get further insights into the physical mechanisms. Northward of the Amundsen continental shelf (i.e., north of the 1500 m isobath and south of 69°S, and between 100°W and 135°W), we project a surface ocean warming of 1°C (Fig. S6a), mostly explained by stronger downward heat fluxes (Fig. S6c), as well as a surface freshening of 0.4 g kg^{-1} (Fig. S6b) explained by increased precipitation and possibly less sea ice production (Fig. S6d). The main thermocline is approximately 75 m higher in the future (Fig. S6a), which comes from reduced convective mixing due to less brine rejection as well as horizontal advection (Fig. S6c,d). The ocean below the thermocline is warmed by approximately 0.25°C in the future (Fig. S6a), which is largely explained by horizontal advection from the domain boundaries (Fig. S6c). In comparison, Sallée et al. (2013) reported that the Circumpolar Deep Water warmed by 0.4°C from 1976-2005 to 2070-2099 in the CMIP5-RCP8.5 multi-model mean.

References

Adusumilli, S., Fricker, H. A., Medley, B., Padman, L., & Siegfried, M. R. (2020). Interannual variations in meltwater input to the Southern Ocean from Antarctic ice shelves. *Nature Geosci.*, *13*(9), 616–620.

Depoorter, M. A., Bamber, J. L., Griggs, J. A., Lenaerts, J. T. M., Ligtenberg, S. R. M., van den Broeke, M. R., & Moholdt, G. (2013). Calving fluxes and basal melt rates

of Antarctic ice shelves. *Nature*, *502*(7469), 89–92.

Dutrieux, P., De Rydt, J., Jenkins, A., Holland, P. R., Ha, H. K., Lee, S. H., ... Schröder, M. (2014). Strong sensitivity of Pine Island ice-shelf melting to climatic variability. *Science*, *343*(6167), 174–178.

Jenkins, A., Shoosmith, D., Dutrieux, P., Jacobs, S., Kim, T. W., Lee, S. H., ... Stammerjohn, S. (2018). West Antarctic Ice Sheet retreat in the Amundsen Sea driven by decadal oceanic variability. *Nature Geosc.*, *11*, 733–738.

Joughin, I., Shapero, D., Dutrieux, P., & Smith, B. (2021). Ocean-induced melt volume directly paces ice loss from Pine Island Glacier. *Science advances*, *7*(43), eabi5738.

Jourdain, N. C., Mathiot, P., Merino, N., Durand, G., Le Sommer, J., Spence, P., ... Madec, G. (2017). Ocean circulation and sea-ice thinning induced by melting ice shelves in the Amundsen Sea. *J. Geophys. Res. Oceans*, *122*(3), 2550–2573.

Little, C. M., & Urban, N. M. (2016). CMIP5 temperature biases and 21st century warming around the Antarctic coast. *Ann. Glaciol.*, *57*(73), 69–78.

Martin, T., & Adcroft, A. (2010). Parameterizing the fresh-water flux from land ice to ocean with interactive icebergs in a coupled climate model. *Ocean Model.*, *34*(3), 111–124.

Meijers, A. J., Shuckburgh, E., Bruneau, N., Sallée, J.-B., Bracegirdle, T. J., & Wang, Z. (2012). Representation of the Antarctic Circumpolar Current in the CMIP5 climate models and future changes under warming scenarios. *J. Geophys. Res. Oceans*, *117*(C12).

Rignot, E., Jacobs, S., Mouginot, J., & Scheuchl, B. (2013). Ice-shelf melting around

Antarctica. *Science*, *341*(6143), 266–270.

Sallée, J. B., Shuckburgh, E., Bruneau, N., Meijers, A. J., Bracegirdle, T. J., Wang, Z., & Roy, T. (2013). Assessment of Southern Ocean water mass circulation and characteristics in CMIP5 models: Historical bias and forcing response. *J. Geophys. Res. Oceans*, *118*(4), 1830–1844.

Seroussi, H., Nowicki, S., Payne, A. J., Goelzer, H., Lipscomb, W. H., Abe-Ouchi, A., ... others (2020). ISMIP6 Antarctica: a multi-model ensemble of the Antarctic ice sheet evolution over the 21st century. *The Cryosphere*, *14*(9), 3033–3070.

Spence, P., Griffies, S. M., England, M. H., Hogg, A. M., Saenko, O. A., & Jourdain, N. C. (2014). Rapid subsurface warming and circulation changes of Antarctic coastal waters by poleward shifting winds. *Geophys. Res. Lett.*, *41*(13), 4601–4610.

Wang, Z. (2013). On the response of Southern Hemisphere subpolar gyres to climate change in coupled climate models. *J. Geophys. Res. Oceans*, *118*(3), 1070–1086.

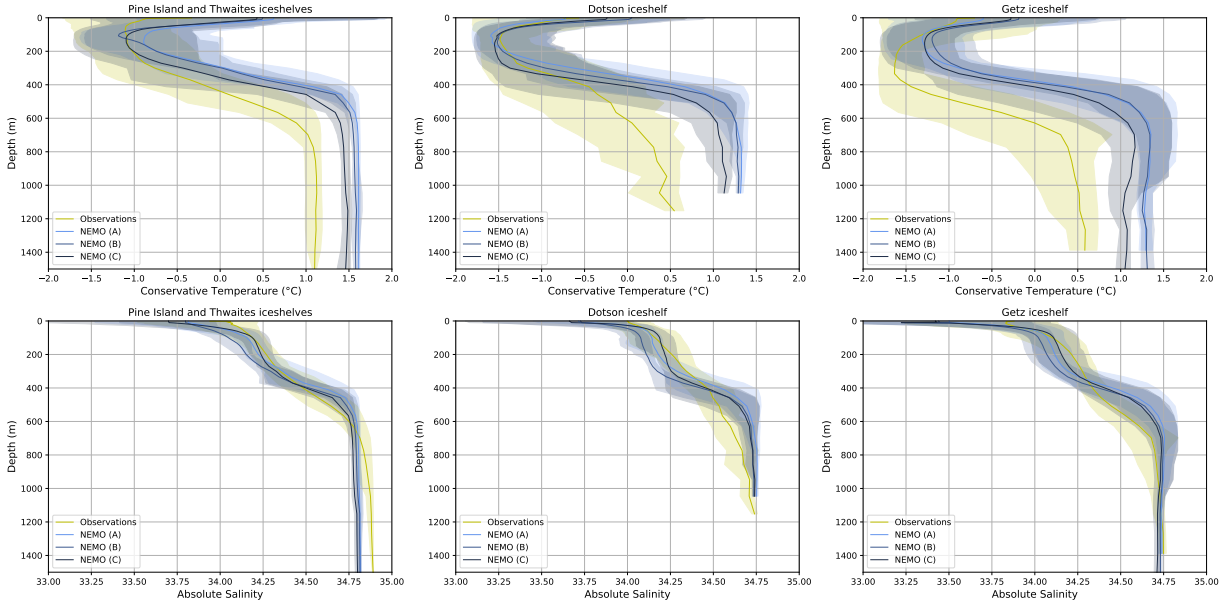

Figure S1. Vertical temperature and salinity profiles averaged in front of Pine Island and Thwaites (108-100°W, 76-74°S), Dotson (114-111°W, 75-73°S) and Getz (135-114°W, 75-73°S, over the continental shelf) from observational data (see text) and model configurations A, B and C. The model profiles are co-located in space and time with the observational profiles (linear interpolations based on monthly model outputs). The shaded semi-transparent areas indicate the 5^{th} and 95^{th} percentiles over all co-located profiles.

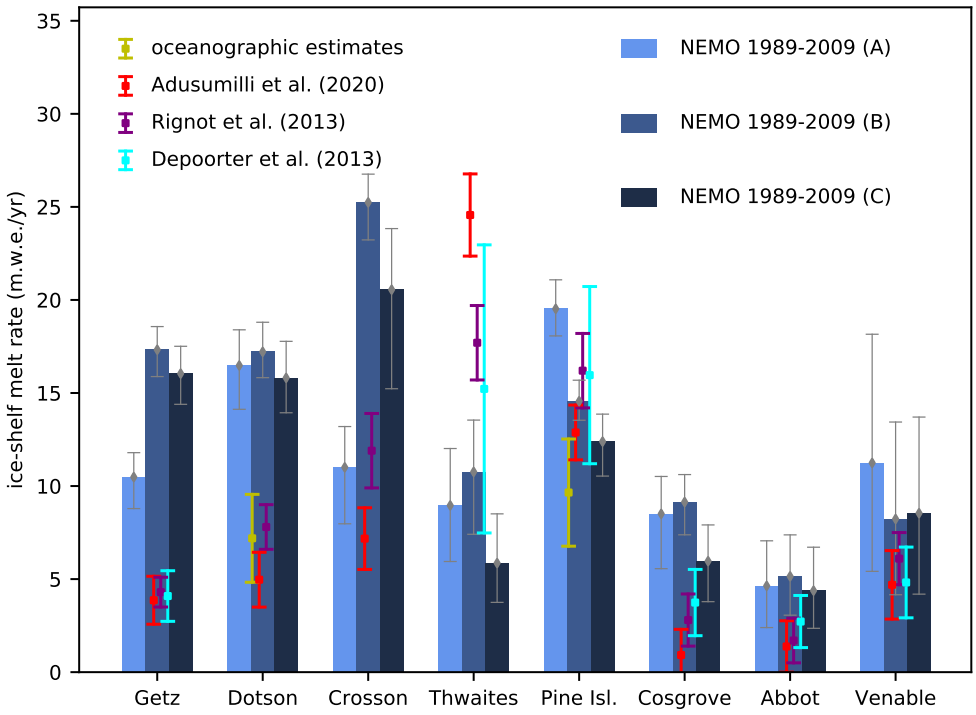

Figure S2. Comparison of simulated (large blue bars) and observation-based (thin colored bars) melt rates beneath individual ice shelves. Oceanographic estimates represent summers of early 1994, 2007, 2009, 2010, 2012, and 2014 for Pine Island (Joughin et al., 2021) and summers of early 2000, 2006, 2007, 2009, 2011, 2012, 2014 and 2016 for Dotson (Jenkins et al., 2018). The other observational estimates are based on satellite observations combined with firm simulations and represent the 2003-2008 period for Rignot et al. (2013) and Depoorter et al. (2013) and 1994-2018 for Adusumilli et al. (2020). The observational error bars show the 95% confidence interval based on 10^6 calculations of the multi-year mean, using random samples in normal distributions for individual years with standard deviations provided by Joughin et al. (2021) and Jenkins et al. (2018). The 95% interval for Rignot et al. (2013) and (Depoorter et al., 2013) was calculated from the provided standard deviation assuming a normal distribution. Grey bars indicate 95% of model monthly outputs (i.e. leaving out the 2.5% lowest and 2.5% highest values).

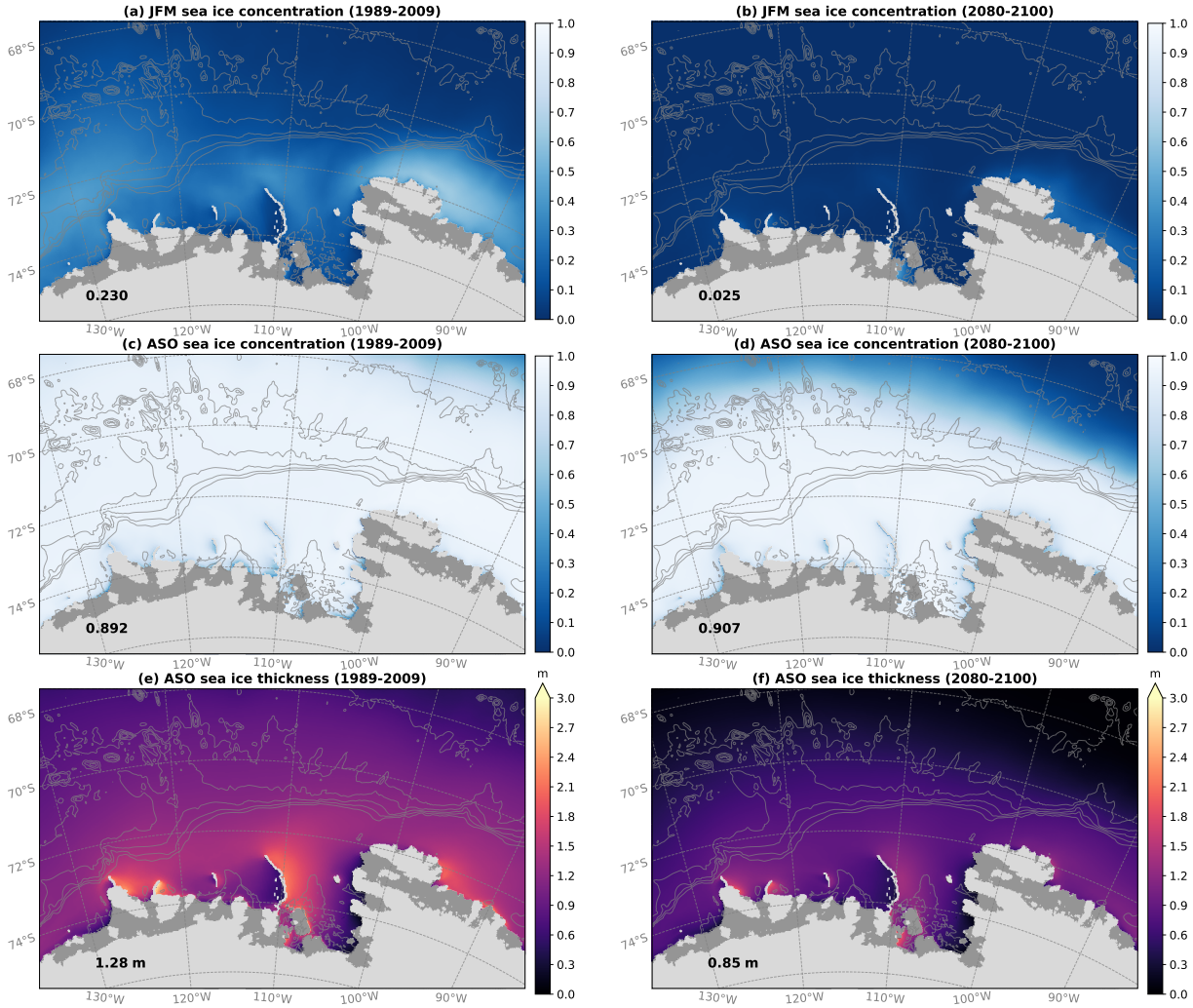

Figure S3. Sea ice concentration and thickness in austral summer (JFM) and late austral winter (ASO) for present day and future simulations. Numbers near the lower left corner indicate values integrated over the continental shelf defined as the area between the 1500 m isobath and the coastline, and between 100°W and 135°W.

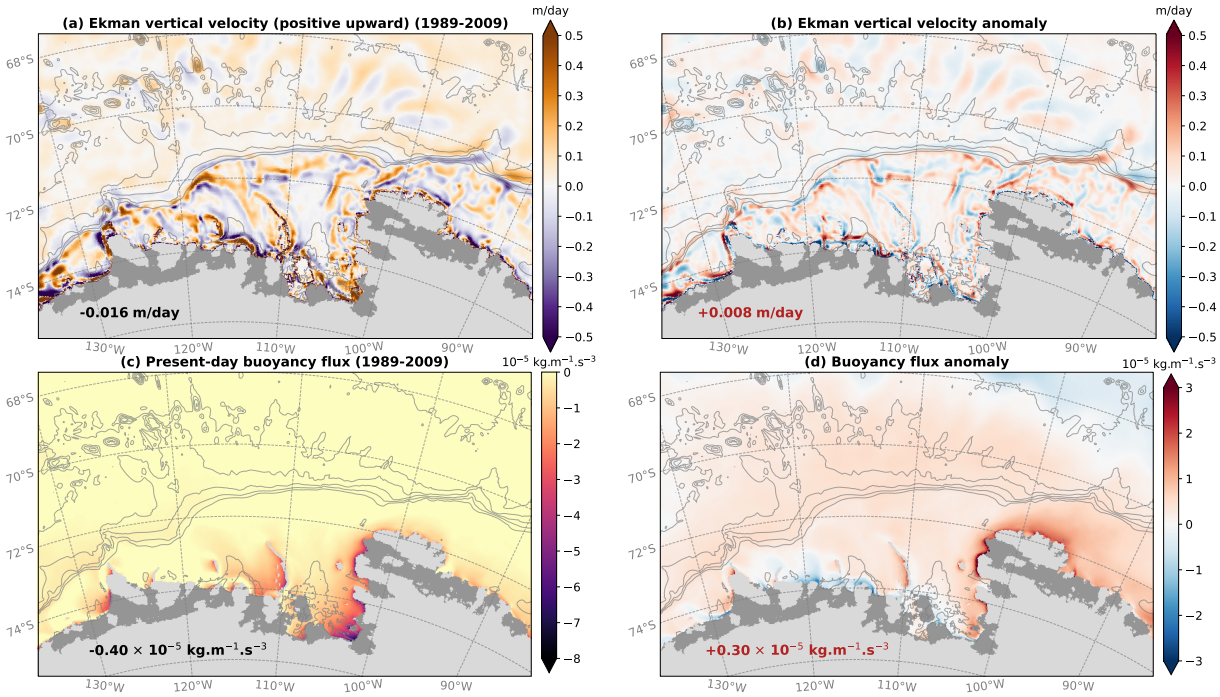

Figure S4. Present-day (left) and future anomaly (2080–2100 minus 1989–2009) of Ekman vertical velocity (upper) and surface buoyancy flux (lower). Numbers near the lower left corner indicate values averaged over the continental shelf defined as the area between the 1500 m isobath and the coastline, and between 100°W and 135°W.

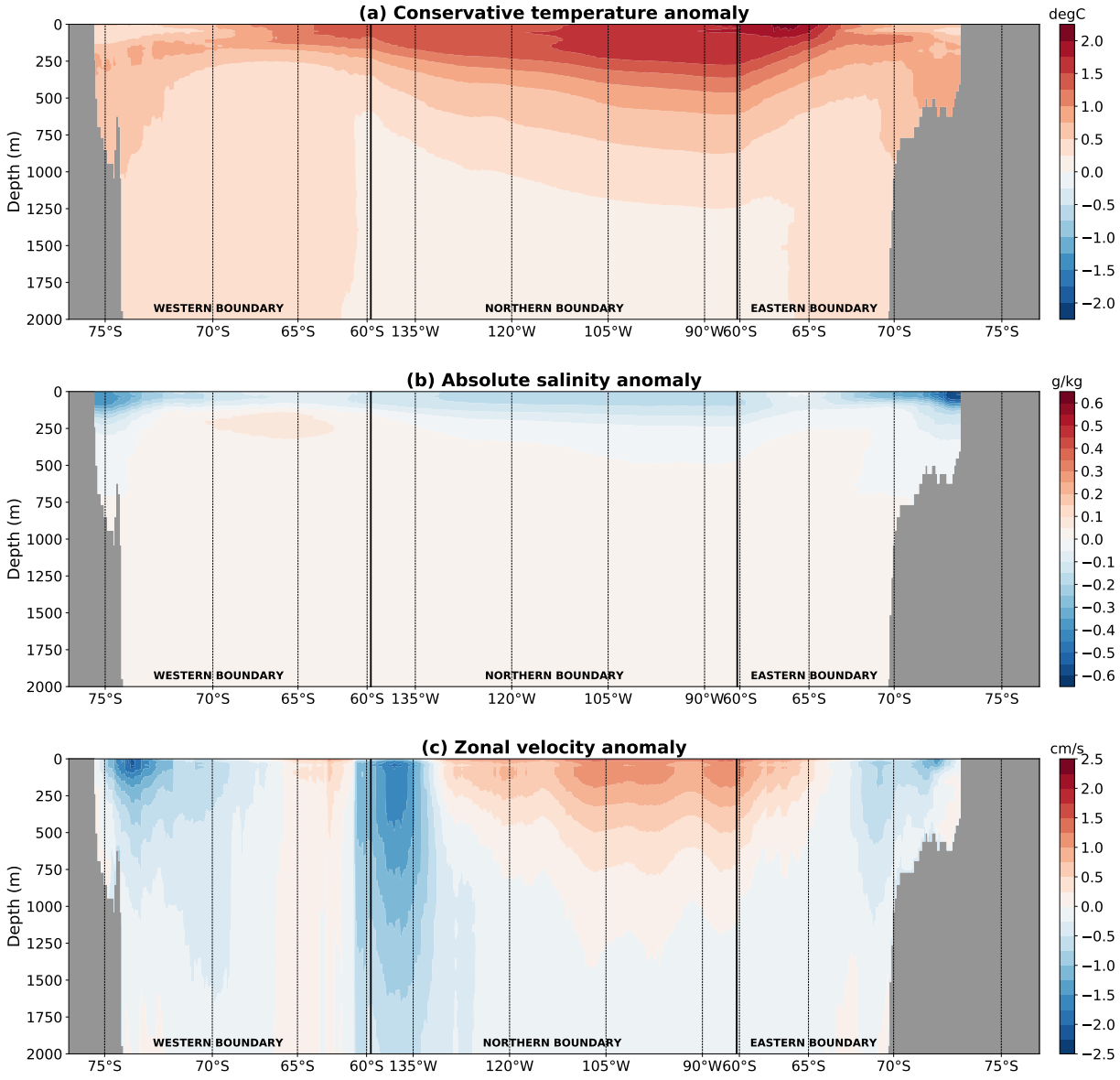

Figure S5. CMIP5 multi-model mean anomalies added to the present-day lateral boundary conditions of (a) conservative temperature, (b) absolute salinity, and (c) zonal ocean velocity. The model bathymetry is shown in grey and only the first 2000 m are shown.

Table S1. Changes in ice shelf melt rates found in NEMO simulations A, B and C (1st part), and subsequent increase in calving rate according to the ISMIP6 sensitivity (2nd part). Relative increase in calving rate compared to present-day (3rd part) and relative increase in iceberg melt due to both increased calving and increased erosion by a warmer ocean (4th part).

	A	**B**	**C**
Increase in ice shelf melt ($\mathbf{Gt.yr^{-1}}$)			
Crosson–Dotson	+174	+124	+189
Getz	+121	+156	+199
Increase in iceberg calving ($\mathbf{Gt\,yr^{-1}}$)			
Crosson–Dotson	+125	+89	+136
Getz	+22	+28	+36
Relative increase in calving			
Crosson–Dotson	+95%	+67%	+103%
Getz	+39%	+59%	+64%
Relative increase in iceberg melt			
Crosson–Dotson	+195%	+167%	+203%
Getz	+139%	+159%	+164%

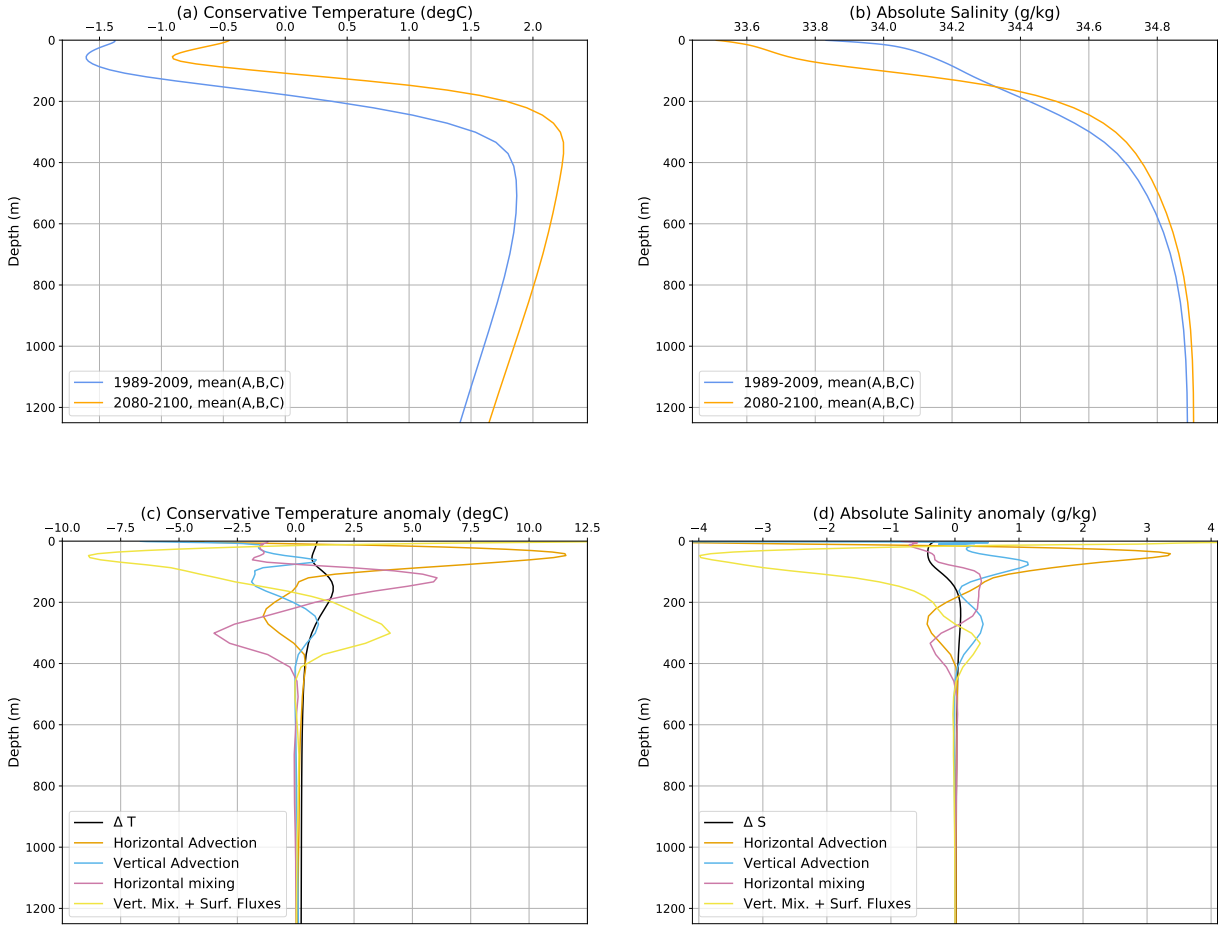

Figure S6. (a,b) Present-day and future conservative temperature and absolute salinity profiles offshore of the Amundsen Sea continental shelf (average north of the 1500 m isobath and south of 69°S, and between 100°W and 135°W). (c,d) temperature (ΔT) and salinity (ΔS) change from present-day to future conditions and contributions of the individual terms of the heat and salt equations to ΔT and ΔS, respectively.